PHYSICAL REVIEW C **68**, 064004 (2003)

Experimental study of the $^{12}C(K^-_{stopped}, \pi^0)^{12}_{\Lambda}B$ reaction

M. W. Ahmed,* X. Cui, A. Empl, E. V. Hungerford, K. J. Lan, and M. Youn†
University of Houston, Department of Physics, 4800 Calhoun, Houston, Texas 77204-5506, USA

R. E. Chrien, R. Gill, P. Pile, A. Rusek, and R. Sutter
Brookhaven National Laboratory, Department of Physics, Upton, New York 11973, USA

J. Bjoraker, D. Dehnhard, J. M. O'Donnell,‡ J. Gerald, H. Juengst, and J. H. Liu
University of Minnesota, School of Physics & Astronomy, 116 Church Street SE, Minneapolis, Minnesota 55455, USA

J. C. Peng,§ C. L. Morris, C. M. Riedel,‖ and H. A. Thiessen
Los Alamos National Laboratory, Los Alamos, New Mexico 87545, USA

D. Androic, I. Bertovic, M. Furic, T. Petkovic, and M. Planinic
University of Zagreb, Department of Physics, Bijenicka 32 HR-10000 Zagreb, Croatia

L. Tang
Hampton University, 12000 Jefferson Avenue, Newport News, Virginia 23606, USA

V. Zeps
University of Kentucky, Department of Physics, Lexington, Kentucky 40506, USA

(Received 22 November 2002; published 31 December 2003)

The $(K^-_{stopped}, \pi^0)$ strangeness and charge changing reaction was investigated by producing a $^{12}_{\Lambda}B$ hypernucleus from a carbon target. The branching ratio for K^- capture to the ground and *p*-shell states of this hypernucleus was found to be $(0.28\pm0.08)\times10^{-3}$ and $(0.35\pm0.09)\times10^{-3}$, respectively, which after correction for isospin was lower than a previously measured value for the $^{12}C(K^-_{stopped}, \pi^-)^{12}_{\Lambda}C$ reaction, but still above the theoretical predictions for the ground state. The experiment obtained a missing-mass resolution comparable to in-flight reactions, however the higher background and lower selectivity of the $K^-_{stopped}$ reaction limits its usefulness in the study of new hypernuclear species.

DOI: 10.1103/PhysRevC.68.064004 PACS number(s): 21.80.+a, 21.10.Dr, 21.60.Cs

I. INTRODUCTION

A hypernucleus is a bound, many-body system in which SU(3)-flavor symmetry may be expected to play an important role. Although nuclear systems containing more than one hyperon are predicted to be stable [1], only Λ and Σ hypernuclei have been conclusively observed, and only the spectroscopy of single Λ hypernuclei studied in detail.

Most previous spectroscopic studies of hypernuclei have used the mesonic reactions [2], (K^-, π^-) and (π^+, K^+) which replace a neutron in a nuclear target by a Λ. However, new hypernuclear species can be created by using charge as well as strangeness changing reactions, such as $(e, e'K^+)$ or (K^-, π^0). These latter processes replace a proton in a nucleus by a Λ. We here report on the results of an experimental study on the usefulness of the $(K^-_{stopped}, \pi^0)$ for the production of hypernuclei, charge symmetric to those previously studied by in-flight, mesonic reactions.

In general, comparison of the spectra of charge symmetric hypernuclei provides information needed to extract the charge asymmetry of the fundamental Λ-nucleon interaction. This has been studied to some extent in the ground states of *s*- and *p*-shell mirror hypernuclear pairs, but aside from binding energies, few comparative data are available [3]. However in addition to charge asymmetry in the fundamental Λ-*N* interaction, first-order Coulomb effects can lead to energy differences between isospin symmetric hypernuclei, in part because the addition of a Λ to the nuclear core changes its radius [4]. Therefore a careful study of the spectra of several charge symmetric pairs is needed to extract both the Coulomb and charge asymmetry effects for the excited as well as the hypernuclear ground states. Indeed, if the Coulomb energy contributions are understood, it would be possible to extract a hypernuclear radius from these data [5].

*Corresponding author. Present address: Triangle Universities Nuclear Laboratory, Duke University, Durham, NC 27708. Email address: mohammad.ahmed@duke.edu
†Present Address: Inst. of Physics and Applied Physics, Yonsei University, Seoul 120-749, Korea.
‡Present Address: LANSCE-3, MS H855, Los Alamos, NM 87545.
§Present Address: Department of Physics, University of Illinois at Urbana-Champaign, Urbana, IL 61801.
‖Present address: Montana State University, Dept. of Physics, Bozeman, MT 59717.

A. Production of hypernuclei

Hypernuclei are produced by introducing strangeness into a nucleus. The transfer of strangeness can occur by (1) strangeness exchange, i.e., an up or a down quark in a nucleon is exchanged for a strange quark, or (2) associated production, where a strange and an antistrange quark are simultaneously produced with only the strange quark remaining in the nucleus. The experiment discussed here uses the strangeness exchange process.

In the reaction of interest, a low-momentum, negative kaon beam is brought to rest in a nuclear target. Stopped kaons are used because essentially all stopped K^- interact with the nuclear target, and the initial momentum can be assumed to be zero. In addition, the stopped beam also allows thick targets to be used without degrading the energy resolution, as the outgoing particles are photons from π^0 decay.

The reaction proceeds when a kaon is absorbed from an atomic orbit into the nucleus. X-ray measurements of kaon absorption on ^{12}C [6], for example, indicate that ~55% of all the kaons are captured from 3*d* orbits, while the remaining half are believed to be captured from low angular momentum, l_k=0 or 1, and large n_k states. During capture, a Λ is produced by the reaction $K^- + N \rightarrow \Lambda + \pi$ or by decay of Σ's produced in a similar K^- capture reactions. Kaon absorption at rest provides momentum transfer approximately equal to the Fermi momentum of a bound Λ, and for a C target, angular momentum transfers $J \leqslant 4$ are possible [7].

B. Hypernuclear spectroscopy

The acquisition of hypernuclear binding energies, well depths, and positions of the hypernuclear levels began in the 1960s. Early work included K^- absorption in emulsions and bubble chambers where hyperfragments were identified by their mesonic decays. These efforts successfully established the binding energies of a number of light hypernuclei [8,9].

Most recent hypernuclear studies have taken advantage of intense, separated kaon beams and missing-mass spectrometers to produce hypernuclei with in-flight reactions such as (K^-, π^-) [10,11] or more recently (π^+, K^+) [12,13]. From these studies, the excited as well as the ground state energies are observed.

However, the first hypernuclear counter experiments used the $(K^-_{\text{stopped}}, \pi^-)$ reaction because of the low intensity of the kaon beam lines then available. In the first such experiment [14] a kaon beam was brought to rest in a carbon target, and following the absorption of the kaon, a $^{12}_{\Lambda}$C hypernucleus was formed and identified by the emission of a π^-. Two broad peaks were observed in the pion spectrum, one with a B_Λ =11±1 MeV and the other with B_Λ=0±1 MeV [15]. The widths were dominated by the experimental resolution, 6±1 MeV/*c*, and the production rates of the two peaks, subsequently identified as Λ *p*- and *s*-shell hypernuclear states in $^{12}_{\Lambda}$C, were $(2\pm1)\times10^{-4}$ and $(3\pm1)\times10^{-4}$ per stopped kaon, respectively.

In another K_{stopped} experiment, the $^{12}\text{C}(K^-_{\text{stopped}}, \pi^-)^{12}_{\Lambda}\text{C}$ was observed at KEK [16], where it was found that the probabilities per stopped kaon for the formation of *s*-shell and *p*-shell states were $(0.98\pm0.12)\times10^{-3}$ and $(2.3\pm0.3)\times10^{-3}$, respectively. These formation probabilities were a factor of 3 larger than the values calculated by Gal [17] and Bando [18], and a factor of 8 larger than the Matsuyama-Yazaki [19] predictions. However, the relative strengths between the two peaks were found to be in better agreement with theory.

The availability of the Neutral Meson Spectrometer (NMS) [20] which is a large acceptance π^0 detector, and the intense kaon beams at the Alternating Gradient Synchrotron provided an opportunity to study the charge as well as strangeness changing reaction, $^{12}\text{C}(K^-_{\text{stopped}}, \pi^0)$, which produces hypernuclei charge symmetric to most of those previously studied.

More recently a theoretical study of the in-medium modification of the $\bar{K}N$ interaction points out that the $(K^-_{\text{stopped}}, \pi)$ reaction can be used to better define the K^- optical potential at threshold. New estimates of the branching ratios for $(K^-_{\text{stopped}}, \pi)$ were produced using a K^-N *t* matrix constructed within a coupled-channel chiral model [21].

II. THE EXPERIMENT

A. The observables

The energy levels of $^{12}_{\Lambda}$B, resulting from coupling a Λ to a $S_{1/2}$ or a $P_{3/2}$ state of the ^{11}B core nucleus, are observed by measuring the total energy of the ejected π^0 after K^- absorption. As the π^0 decays into two photons [BR =(98.798±0.032)%, BR stands for branching ratio] its momentum must be inferred from its decay kinematics.

The total energy of the π^0, ω can be written in the form

$$M^2_{\pi^0} = \frac{1-\chi^2}{2}\omega^2(1-\cos\,\eta),$$

$$\omega = \sqrt{\frac{2M^2_{\pi^0}}{(1-\cos\,\eta)(1-\chi^2)}},$$

$$\chi = \frac{E_{\gamma_1} - E_{\gamma_2}}{E_{\gamma_1} + E_{\gamma_2}}, \tag{1}$$

where M_{π^0} is the pion mass, η is the opening angle between the two photons in the π^0 decay, and $E_{\gamma1}, E_{\gamma2}$ are the photon energies. For small relative asymmetry between the photon energies, χ, it can be seen that ω is sensitive to the more accurately determined opening angle, and only sensitive in second order on the ratio of the relative energy difference between the photons, $(1-\chi^2)$. In this experiment most of the data analysis and simulations were performed with a $|\chi| \leqslant 0.2$.

B. Beam-line apparatus

The experiment used the low-energy separated beam line (LESBII-C8) at the Alternating Gradient Synchrotron (AGS) at Brookhaven National Laboratory. A dispersed kaon beam (K^+ for calibration and K^- for the reaction of interest) with a nominal momentum of 690 MeV/*c* was brought to rest in a set of four natural graphite targets after it traversed a wedge-

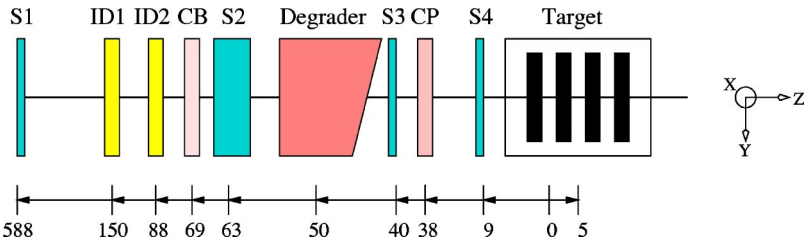

FIG. 1. (Color online) Schematic of E907 beam line. The distances are in centimeter.

shaped, brass degrader of central thickness ~141 mm. The targets, each 12.7 mm thick, were components of an Active Target Chamber (ATC) system [22], which provided the transverse as well as longitudinal coordinates of the stopped kaons.

1. The beam line

Kaons in the C8, LESB-II channel were produced in a 9-cm-long Pt target by the primary proton beam from the AGS. The C8 beam line is 1500 cm long with an angular acceptance of 10 msr and a 5% momentum acceptance. The kaon beam from the production target is momentum selected, filtered by two $E \times B$ separators for kaon to pion separation, and then collimated and focused onto the degrader. Just upstream of the degrader (Fig. 1) the beam traversed two drift chambers ID1 and ID2, a scintillator S2, and a pion threshold Čerenkov detector CB. The beam also passed through a timing scintillator S1 placed just downstream of the mass slit of the separator system.

2. The beam tune

The beam was tuned for a dispersed focus at the degrader with a nominal momentum of ~690 MeV/c. The relative momentum spread $\Delta p/p$ was ±5%. The wedge-shaped degrader was used to compensate for the beam dispersion (~1.2 MeV/c/cm) as predicted by a Monte Carlo simulation of the beam dynamics. It was constructed with a wedge angle of 4.2° with central thickness of 14.1 cm, and was designed to bring the momentum dispersed beam to rest in the stopping targets ~100 cm downstream.

The momentum tune maximized the number of kaons stopping in the carbon targets. This optimization was accomplished by observing the residual beam in a stack of 12 scintillators placed immediately downstream of the target, as the momentum was changed in (discrete) steps, between ≈640 and 708 MeV/c. Stopping kaons had large energy loss, so by observing the pulse height in each scintillator the stopping position was inferred. At momenta over 700 MeV/c, kaon signals were seen in all 12 scintillators, but as the momentum was decreased, the kaon signal in the downstream scintillators disappeared. An optimized tune was reached when the number of kaons in S4, the scintillator just upstream of the target, was maximized while the strength of the kaon signal associated with large energy loss in the scintillator downstream of the target was minimized.

3. Particle identification and beam triggers

There were predominantly two types of beam triggers implemented in the experiment: (1) a kaon beam (K beam) trigger, and (2) a pion beam (π beam) trigger. K beam was defined by a coincidence between S1, S2, and a threshold Čerenkov detector CB, veto ($S1 \cdot S2 \cdot \overline{CB}$). The threshold Čerenkov detector provides clean discrimination between pions and kaons by cutting on pulse height. The π beam trigger was then $S1 \cdot S2 \cdot CB$. Due to decays and nuclear interactions between the kaons and the degrader material, typically less than 40% of the kaons incident on the degrader were transmitted to the target.

It was essential to determine whether a kaon (pion) traversed the degrader, and this was done by requiring a coincidence between the K beam (π beam) and S3 which was immediately downstream of the degrader (K/π beam $\cdot$ S3). Since the π beam rate is much higher than that for K beam, it was also necessary to prescale the π beam trigger before its introduction into the trigger sum. Typical π beam scaling was 1/40. Figures 2 and 3 show the time of flight between S1 and S2, and the energy loss spectrum in S3.

As the kaons emerge from the degrader, their maximum kinetic energy is ~60 MeV (Monte Carlo simulation), and a significant number (~50%) decay in flight prior to reaching the target, ≈50 cm downstream of S3. In order to tag the kaons immediately prior to the target, another scintillator S4 was used. The dimensions of S4 were similar to that of the target chamber. However, S4 was entered into the data stream as a tag rather than included as a requirement in the hardware trigger.

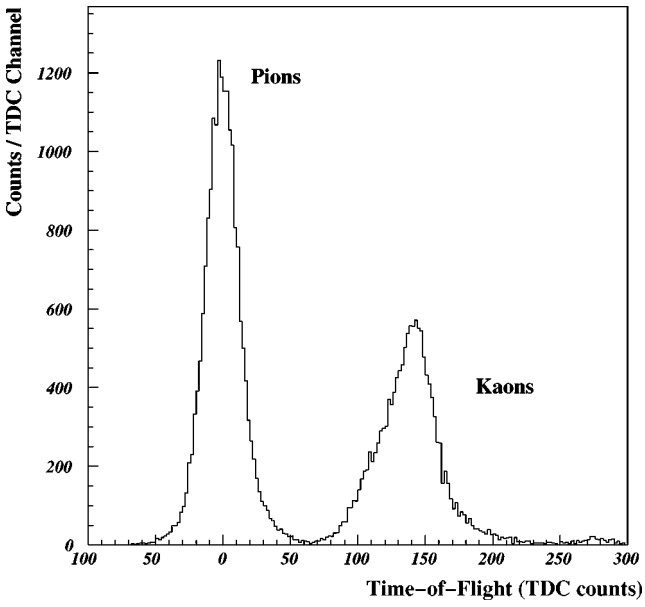

FIG. 2. Time of flight spectrum between S1 and S2 for (K beam $\cdot$ S3) $\cdot$ OR $\cdot$ (prescaled π beam $\cdot$ S3) trigger.

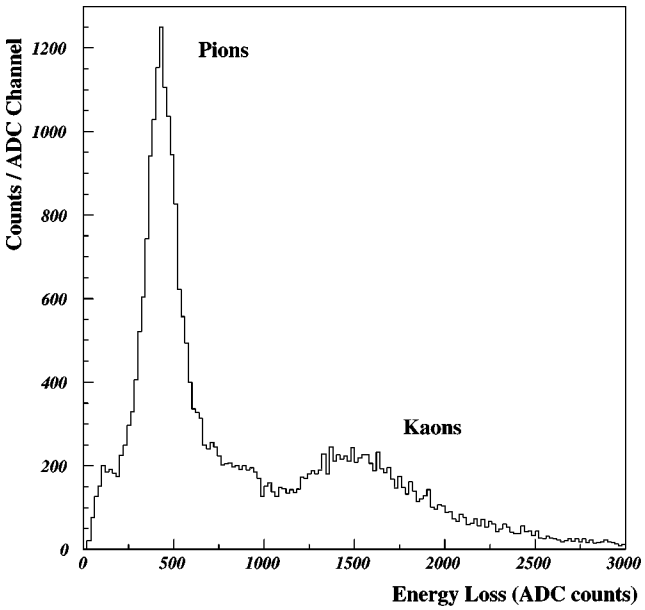

FIG. 3. Energy loss in S3 for $(K\,\text{beam}\cdot\text{S3})\cdot\text{OR}\cdot(\text{prescaled}\ \pi\,\text{beam}\cdot\text{S3})$ trigger.

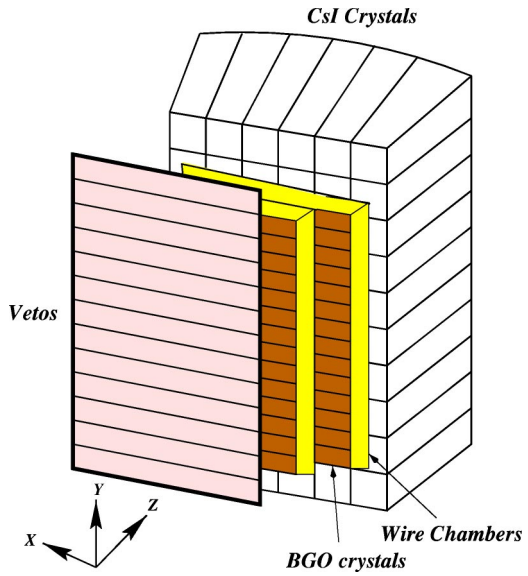

FIG. 4. (Color online) Schematic of one of the NMS arms.

C. The ATC

A Monte Carlo simulation of the π^0 decay process showed that in order to achieve the desired missing-mass resolution ($\leqslant 2\ \text{MeV}/c^2$), the vertices of the stopping kaons must be known with better than 1 mm resolution (σ) in X (vertical to the beam), 2 mm in Y (horizontal to the beam), and less than $\sim$6 mm in Z (the beam direction). Therefore, incoming kaons were tracked to their stopping point with a set of multiwire proportional counters (MWPCs) with a cathode strip readout . Carbon targets were inserted between every second proportional counter so that the ATC contained ten sets of MWPCs with four targets. The construction and performance of the ATC was described in Ref. [22]. It provided the vertex resolution with errors $\sigma_x, \sigma_y, \sigma_z$ of 0.45, 1.18, and 6.35 mm, respectively.

D. The NMS

The NMS measures the total energy of a neutral meson, π^0, by detecting the direction and energy of the γ showers originating in its decay. The NMS consists of two CsI arrays of 60 crystals each, fronted by a set of bismuth germanate (BGO) converter and wire chamber tracking planes. The CsI crystals provide the photon calorimetry to determine the relative energy difference between the decay photons, while the BGO and wire chambers determine the location of the photon conversion. This later position combined with the K^- stopping position from the ATC provides the opening angle between the photons. Figure 4 shows the entire NMS assembly.

1. Veto scintillators

The veto scintillators were used to reject charge particle backgrounds entering the front face of the NMS. There were a total of 14 veto scintillators in each of the NMS arms, covering the entire active area of the CsI crystal array. They were not used in the hardware trigger.

2. Converter planes

The task of a BGO converter plane is to convert the photon into an electron-positron pair which can then be detected by the wire chambers. Each plane consisted of two elements: (1) a BGO strip hodoscope (14 crystals, each 16 in. $\times$2 in. $\times$0.25 in.), and (2) a set of multiwire chambers. The trajectory of the conversion pair can be projected backwards from the wire chamber onto the BGO strip, and thus its spatial origin determined within an error proportional to the thickness of the strip. The shower then enters the CsI crystal array where the remainder of the electromagnetic shower is absorbed.

A set of four wire chambers behind each BGO plane constitutes a chamber package, and consists of four anode planes and four actively read cathode planes. A set of two anode planes and two cathode planes measure two X-positions and two Y-positions. Figure 5 shows a schematic drawing of a chamber package.

3. CsI crystal array

The CsI crystal array lies behind the converter planes. This array measures the energy of an electromagnetic shower. Each of the NMS arms contains an array of 60 CsI crystals (4 in. $\times\sim$4 in. $\times$12 in., having a small horizontal taper). The length of a crystal is chosen to contain $\sim$97% of the total energy of a photon shower with primary energy $\leqslant$800 MeV ($\sim$19 radiation lengths). Each CsI crystal is optically connected to a 3-in. photomultiplier tube (PMT) on its back face, and is optically isolated from the other crystals. The lightguide connecting the crystal and the PMT was also CsI. The entire crystal array is housed in a thick aluminum casing, viewing the target through a thin window behind the converter planes.

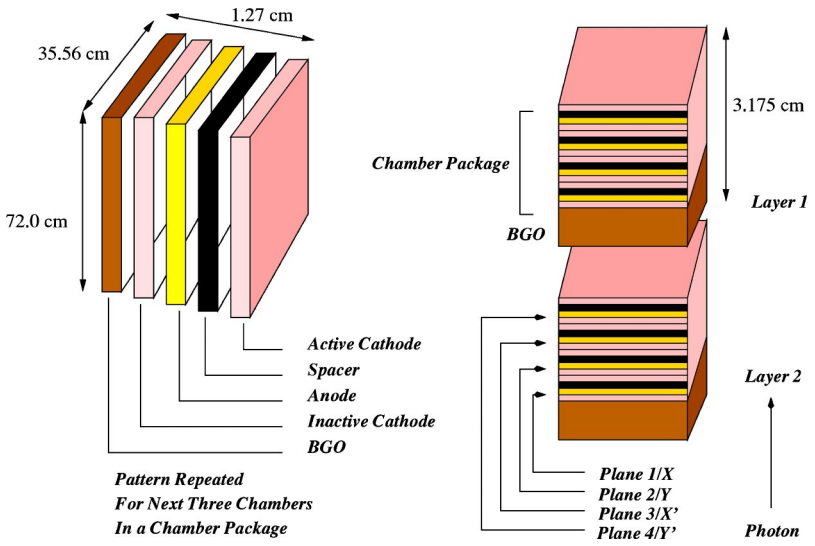

FIG. 5. (Color online) Schematic of NMS chamber package.

E. Data acquisition (DAQ)

The experiment used a PC based data acquisition system [23] NMSDAQ which provided an interface to the National Instruments IEEE standard GPIB data acquisition hardware. The NMSDAQ consisted of two unique programs, the data acquisition DAQ, control program, and a data monitoring program NMSMonitor. The DAQ program was responsible for performing all the necessary calls to the hardware to acquire data, whereas the NMSMonitor program was an independent application, called by the DAQ to display analog to digital convertor (ADC) and time to digital convertor (TDC) histograms of all the channels read out by the DAQ. No data reduction or analysis was handled by the DAQ.

1. DAQ hardware and trigger

The detector readout included all NMS components (CsI crystals, BGO strips, veto scintillators, and wire chambers), and the beam-line components (ATCs), scintillators, Čerenkovs, and drift chambers). The CsI crystals, vetoes, NMS wire chambers, beam-line scintillators, and Čerenkov detector were also used to form the system trigger.

The NMS components were read using FERA [24] ADC/TDC, whereas all the beam-line elements and the target were read using FASTBUS [24] ADC/TDC. However, both types of data were polled into FERA MEMORIES which were then read by the DAQ into the computer. Figure 6 shows the data flow from each of the detector elements.

2. Triggers

There were two trigger levels in the experiment. To obtain the first-level physics trigger, the analog signals from all 60 crystals in each arm of the NMS were summed separately, and this summed output was subjected to a threshold cut controlled by the DAQ. Requiring the CsI in the trigger implied that each NMS arm must have observed an energy larger than this threshold. The CsI trigger could be run in two different modes, singles and coincidence. The singles mode required only one of the two NMS arms to cross the energy threshold, whereas the coincidence mode required both NMS arms to simultaneously have an energy larger than the respective thresholds. It was possible to subject both arms to different thresholds, however this was never done, and during the entire experiment a common threshold was set at 38 MeV for both arms of the NMS.

A veto trigger required a logical OR between any of the 13 vetoes in an arm (Table I). Requiring this trigger reduced the trigger rate, however due to the possibility of vetoing good events which might have an associated charged reaction product or a charged "backsplash" [25] from the CsI, the veto was not inserted in the hardware trigger. A software cut was later used after analysis to exclude events with veto signals.

The second-level trigger was implemented to ensure that the DAQ computer and CAMAC interface hardware were ready to accept data from the ADCs and TDCs. This level of

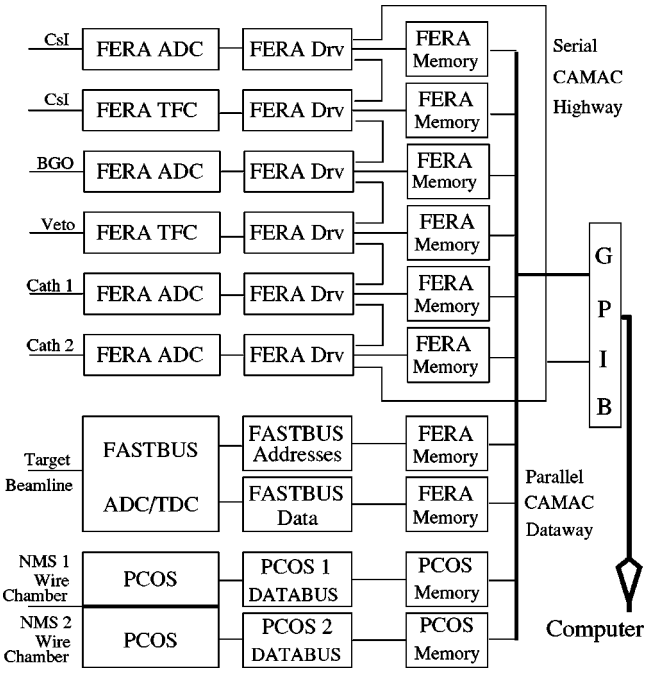

FIG. 6. Data flow diagram for the experiment.

TABLE I. Detector elements which participated in triggering.

Detector element	Decision based upon
CsI crystals	Energy sum of all crystals
Veto scintillator	Timing signal between an OR of all veto signals
NMS chambers	Logical YES/NO between an OR of all chamber wires
Scintillator S1,S2, and S3	ADC pulse height threshold
Čerenkov CB	Threshold set for pions only

trigger was made by polling the busy signals of the FERA modules to make a (BUSY-OR) trigger. This (BUSY-OR) trigger was unset if any one of the FERA ADCs or TDCs were busy in processing data. The trigger also polled the level of FERA MEMORY capacity. The second level trigger was only set when the FERA MEMORY exceeded a preset limit on the amount of data to be stored prior to readout. In addition, the second-level trigger was only generated when the DAQ computer was not busy in processing the already readout events. If both the first- and second-level triggers were true, an event was read into the computer.

In addition to the first- and second-level data acquisition triggers, there was a scalar trigger which read scalar numbers between beam spills, a "header event" trigger that read temperature information in order to maintain the CsI calibration, and a "cosmics" trigger that allowed the readout of cosmic ray tracks in the NMS. A more detailed description of triggers can be found in Ref. [26].

III. CALIBRATIONS

Two types of data were analyzed by the experiment: (1) calibration data for the ATC and the NMS, and (2) data from the $^{12}C(K^-_{stopped}, \pi^0)$ reaction. Calibration data for the ATC were collected in order to adjust the gains of the various cathode strips, whereas the NMS calibration data were obtained predominantly to calibrate the pulse height response of the CsI and the BGO crystals. The outcome of these calibrations was a set of gain files for both the ATC and the NMS detector components for various time periods during the data acquisition. These files were used to adjust the gains during the analysis of the data.

A. ATC calibration

The center-of-gravity (COG) method provided a sufficiently accurate determination of a track position. However, it is sensitive to the relative gains of the cathode strips, so gain alignment of all strips was required. The position of the COG centroid, representing the position of the passing particle ξ is given by

$$\xi = \frac{q\sum_{i=1}^{n} W_i g_i}{q\sum_{i=1}^{n} g_i},$$

where q is the total induced charge over all the strips, W is the fraction of the total charge at position i, and g_i is the relative gain factor between the strips.

The ADC channel number can be written as

$$Q_i^{ADC} = Q_i^{induced} g_i,$$

where Q_i^{ADC} is the measured ADC count, $Q_i^{induced}$ is the charge induced on the cathode strip, and g_i is the gain for the i^{th} cathode channel. To gain match the 1820 different electronic channels, a square voltage pulse, of known height and width, was injected at the input end of each preamplifier, and the peak position Q^{peak} of the Q^{ADC} distribution determined. The gains were determined by

$$g_i = \frac{Q_i^{peak}}{Q^{induced}}.$$

Figure 7 shows the distribution of Q^{ADC} for all the ATC channels for a calibration pulse of ΔV=21 mV and ΔT =200 nsec. The full width at half maximum (FWHM) of the Q^{ADC} distribution without gain calibration is 100 ADC channels, whereas the FWHM of the gain matched distribution is 12 ADC channels. Thus, gain matching greatly improved the positional resolution of the ATC.

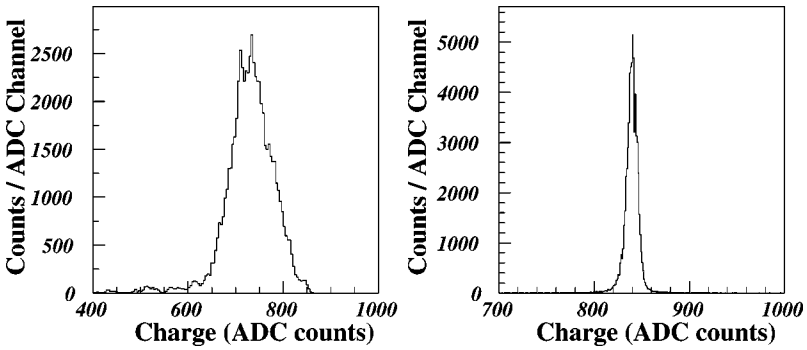

FIG. 7. The distribution of measured charge for all ATC channels is shown. The plot on the left shows the distribution for the case of no gain calibration applied to the channels, and the plot on the right shows the measured charge with gain corrections applied to all channels. The shift in the peak channel number is due to an overall change in the gain settings.

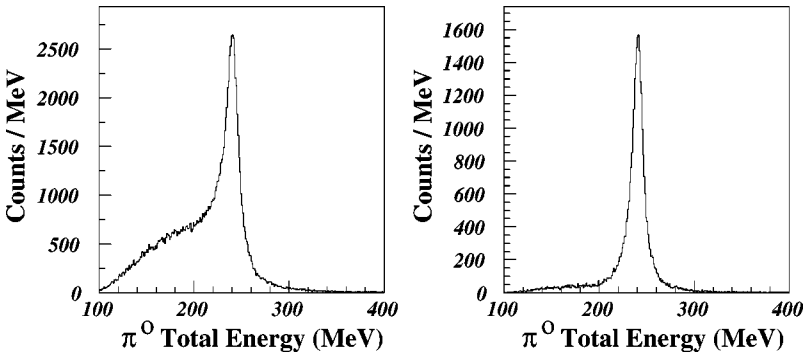

FIG. 8. The total energy of the π^0 using photon conversions in both the CsI and the BGO arrays. The plot on the left shows the energy sum with all events included. The plot on the right shows the same spectrum with the edge crystal cut.

B. NMS calibration

Each NMS wire chamber package contains four cathode planes, and the mechanical construction of the package allows position offset between the planes. To find these offsets, cosmic rays were tracked through the wire chambers. Residuals to a fitted track were obtained and the positions (in X, Y, and Z axes) offset to align the chambers. The cosmic tracks were then refitted, and the process repeated until a minimum in the position residual was obtained. The nominal position residuals for the X planes were $\sigma_x \sim 147$ μm, and for the Y planes $\sigma_Y \sim 120$ μm.

Energy calibration of the CsI and the BGO strips was a multistep process. First, an absolute energy calibration was obtained for all CsI crystals by detecting the monoenergetic π^0 from the $K^+ \rightarrow \pi^+ \pi^0$ decay from K^+ brought to rest in the ATC (BR$\sim$21%). The total energy of the π^0 from this decay is 245 MeV. The task was to match simultaneously the pulse heights from all the CsI crystals to 245 MeV, and to optimize the resolution in this measurement. In order to remove the uncertainty in the BGO converter array's calibrations, only those K^+ data events which had no observed energy deposition in the BGOs were selected for this step in the calibration. The calibration of the CsI arrays has been previously described [27]. Figure 8 shows the total π^0 energy obtained by summing the energy of all the CsI crystals in the NMS. The plot on the left shows the spectrum without cuts on the NMS. The plot on the right shows the energy spectrum obtained from data where the shower centroid did not occur in an edge crystal of the CsI array (*edge crystal cut*). The approximate central location of the shower in the CsI was found by a two-dimensional COG fit to the pulse height from all the crystals in an arm. The shower centroid is usually very close to the center of the crystal which received the largest fraction on the total energy.

The effect of this cut not only improves the energy resolution, but also removes the low-energy tail in the energy spectrum. However it produces a cleaner spectrum at the expense of total acceptance, due to the reduction in the effective geometrical area of the CsI array. The energy resolution obtained for the spectrum with the edge crystal cut is shown in Fig. 9. The standard deviation (σ) of this distribution is $\sim$5 MeV, and corresponds to 2.0% of the 245 MeV deposited in the CsI.

The K^+ data cannot be used to obtain relative energy calibrations for the BGO, since the amount of deposited energy depends on the depth of the conversion in the strip. Therefore, the BGO calibration was based on energy loss of cosmic rays. Unfortunately, the BGO raw ADC values have time variations due to temperature, angle of the track, and the distance along the crystal between the PMT and the location of the scintillation in the crystal. The dependence on the angle and the location of the track can be removed using information from the NMS wire chambers, and corrections due to temperature are described later in this section. Using all this information, the peaks due to the energy deposition by the cosmic rays can be aligned to an arbitrary energy value.

The absolute energy calibration for each layer of BGOs was then obtained using the K^+ decay data by analyzing conversions in one layer of the BGOs at a time, beginning with the inner layers. Since the absolute energy deposited in the CsI is known, the fractional energy deposited in the BGOs relative to the CsI gives the absolute energy calibration of the BGOs. The combined effects of the CsI and BGO calibrations can be observed in the total energy E_{sum} spectrum. Figure 10 shows the E_{sum} spectrum with the CsI edge crystal cut.

The standard deviation (σ) of the total energy spectrum with photon conversion in the BGO crystals is 6.5 MeV. This value is $\sim$1.5 MeV higher than the width of the spec-

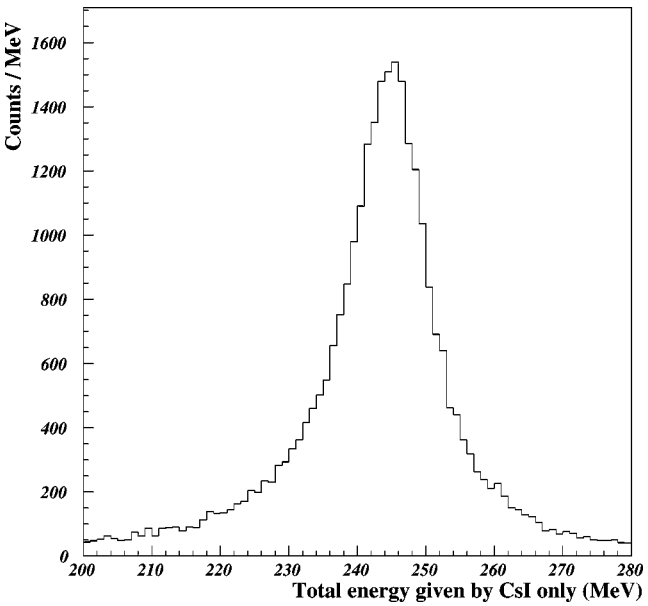

FIG. 9. The total π^0 energy spectrum with photon conversions on CsI only. The σ of the distribution is $\sim$5 MeV.

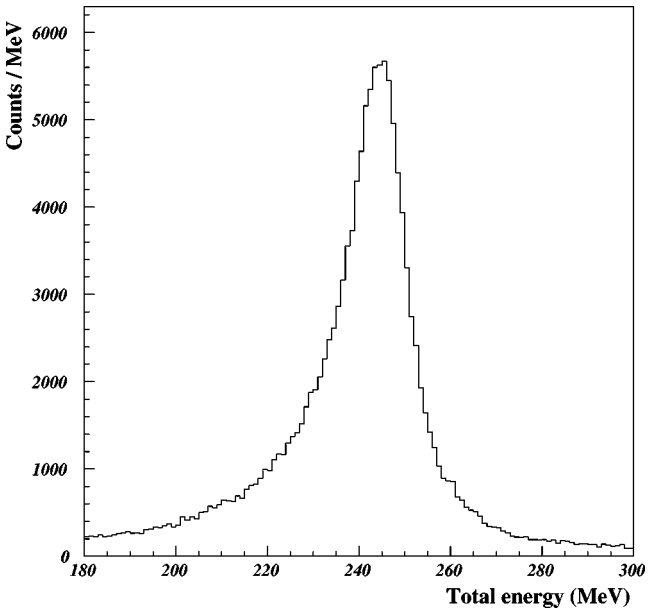

FIG. 10. The total energy of the π^0 as measured by the CsI and the BGO crystals. The σ of the distribution is 6.5 MeV.

trum when the photons converted in the CsI alone, and corresponds to 2.65% of the 245-MeV mean value.

C. Time-based gain drift corrections

Since the data were collected for a long period of time, and over significant temperature variations, the CsI and BGO signals had to be monitored and corrected for electronics drift as well as crystal/PMT gain response as a function of time. Once all the crystals (CsI and BGO) were gain calibrated with respect to one another and an absolute energy calibration was reached, cosmic-ray data were used to monitor any drifts in the energy signals. The cosmic-ray data collected in sets of ~12 h were analyzed for every CsI and BGO crystal and a set of new gain files was obtained for CsI and BGO. This resulted in a set of gain files separated by ~12 h. The gain values from these files were then interpolated in time on an event by event basis during the replay of the data.

IV. DATA ANALYSIS AND RESULTS

A. Monte Carlo simulation

A GEANT based Monte Carlo (MC) simulation program was developed to study the ATC and the NMS response. For the case of the ATC, a TURTLE [28] beam input to the MC at a nominal momentum of 690 MeV/c was generated. The beam vectors were specific to the C8 beam line at the AGS. The MC calculated (1) the number of kaons which enter the ATC, (2) the fraction of the beam which stops in the ATC, and (3) the software tracking efficiency.

In order to make the MC realistic, exact ATC dimensions, materials, and positions of the ATC were used. In addition, induced charge profiles for the cathode strip chambers (CSCs) were obtained from data and used in order to generate hit patterns on the CSCs for the software tracking routines. Since there were no detectors placed between S4 and the ATC, we rely on the MC to determine the acceptance of kaons leaving S4 and entering the ATC, (88±4)%.

The number of kaons stopped in the ATC is governed by the energy loss of kaons in the target material. Since energy loss is purely electromagnetic, the number of stopped kaons is, except for a small correction, independent of the polarity of the kaon beam. Therefore in order to estimate the number of stopped kaons, the MC tracked positive kaons to avoid invoking nuclear interactions in the simulation. From the fraction of kaons entering the ATC, (68±10)% were anticipated to stop in the target. The large error in this number is due, in part, to the uncertainty in the mean momentum and momentum bite in the beam.

A pattern recognition code (PRC) was developed to track the kaons to their stopping vertices. A detailed description of the PRC can be found in Ref. [22]. The MC provided *hit* positions for incident kaons and their actual stopping positions. The hits were then formatted as the real data files and processed through the PRC, stopping vertices calculated, and compared to the stopped positions provided by the MC. It was found that ~91% of the events were reconstructed within the residual error of the target thickness. This exercise validated the software tracking routine used to identify the stopping kaons.

The global structure of the pion energy spectrum is shaped by the NMS solid angle acceptances. Therefore, it was important to know the NMS solid angle as a function of the pion energy, as well as the energy sharing between the two photons. A complete description of the NMS detectors was coded into the MC. Then an isotropic distribution of π^0's in X and Y positions was taken at the four carbon target locations in the ATC. The position of the NMS arms was defined by the rotation matrices obtained through the laboratory survey of the detector elements. The effective solid angle acceptance of the NMS, $\Omega/4\pi$, at an energy sharing parameter of χ=0.2 for η of 66° and 55° (at pion energies of 245 MeV and 307 MeV, respectively) were found to be 0.000 914 and 0.001 15, respectively.

Using the K^+ decay data, the hit multiplicities and patterns between the data and MC were also compared and found to be in good agreement.

B. Number of *K* stops

A total of 3.649×10^9 K beam·S3 triggers were analyzed for the hypernuclear production reaction. However, the number of kaons stopped in the carbon target was not equal to the number of K beam·S3 triggers. A correlation of S2 and S3 counters for purely beam triggered data indicates (73±2)% of the events from the S3 counter were kaon signals. In addition, the ATC was located ~50 cm downstream of the S3 counter. Therefore, the number of kaons emerging from S3 that reach the target must be corrected for decays and outscattering. To do this, the ratio of kaons at S4 compared to those at S3 was extracted by identifying kaons by their energy loss in these scintillators, as observed in their respective ADC spectra. Then the number of kaons emerging from S4 and reaching the C planes in the ATC was estimated by

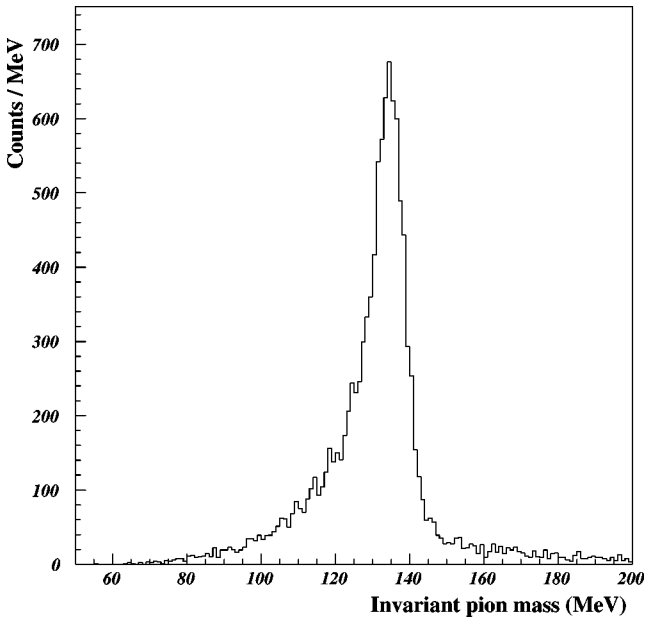

FIG. 11. Invariant π^0 mass. The mean value is 134.5 MeV, and the FWHM ~10 MeV.

Monte Carlo. The values obtained for these two steps were (61±3)% and (88.5±4)%, respectively, for a total of (54±4)%. The predominant contribution to the errors comes from the momentum uncertainty of the beam. The number of kaons stopped in the target was also studied using Monte Carlo simulation, with the result that 68% of the kaons are expected to stop in the target. The number of kaons registered in the ATC were also counted and found to be in agreement with the simulated number given the uncertainties in the knowledge of the momentum and momentum spread of the beam. The number of stopped kaons in the target as determined from the number of K beam triggers corrected by the above factors $(0.73\times0.61\times0.885\times0.68=0.268)$ is $(0.977\pm0.019)\times10^9$.

C. K^+ decay data

The invariant mass spectrum of the π^0 depends directly on the square root of the product of the two photon energies. Thus the error in the missing mass is predominantly due to the error in the energy calibrations. On the other hand, the error in the energy measurement depends to first order on the error in the opening angle, and only secondarily on the calorimetry. The invariant mass is shown in Fig. 11.

It has a FWHM of 10 MeV with a radiative tail. The invariant mass can be used to reject backgrounds due to uncorrelated photons, or those not associated with π^0 decays. Figure 12 shows the opening angle spectrum with and without a missing mass cut. The limit on the opening angle for 245-MeV pions, given the NMS geometry, is 66.6°. Without the missing-mass cut, one finds 26% of the events below this limit. However the application of a missing-mass cut of 10 MeV reduces this percentage to 12%. We also note that the opening angle and energy sharing fraction χ are correlated. It is therefore essential to understand the cuts as applied to the K^+ spectrum before they are applied to the hypernuclear data.

Applying a cut on the energy sharing parameter χ improves the energy resolution and background rejection at the expense of acceptance. For an χ=0.5 the π^0 energy resolution with all cuts is 2.6 MeV (FWHM). If this cut is reduced to 0.1 the resolution improves to 1.74 MeV. The cut also improves the spectrum by removing tails on the missing-mass peak. A Monte Carlo study has shown that these tails are due to in-flight decays and π^0 contamination from other decay channels. Background is also rejected by requiring that the beam track projects back onto the beam scintillator S3.

D. The $^{12}C(K^-_{stopped}, \pi^0)$ spectrum

The total energy spectrum of the π^0 emitted in this reaction is shown in Fig. 13. The region of the spectrum containing the hypernuclear spectra is replotted in Fig. 14. This region is fit by minimizing a function containing two Gaussian peaks added to a linearly increasing background which is superimposed on a constant background of 1.8 counts per MeV. The widths of the Gaussian peaks are required to be equal, but their area, position, and background parameters are allowed to vary. The χ square of the fit was 9.3 for 20° of freedom. It yields a strength of 13.7±4.0 counts for the ground state at 308.2±0.2 MeV, and 17.5±4.5 counts for the $(P^{-1}_{3/2}, \Lambda_P)$ at 298.0±0.5 MeV. The energy resolution extracted from the fit was 2.2 MeV.

In order to calculate the binding energy of the hypernuclear ground state as well as the transition probability per stopped kaon, the various efficiencies and acceptances described below were used.

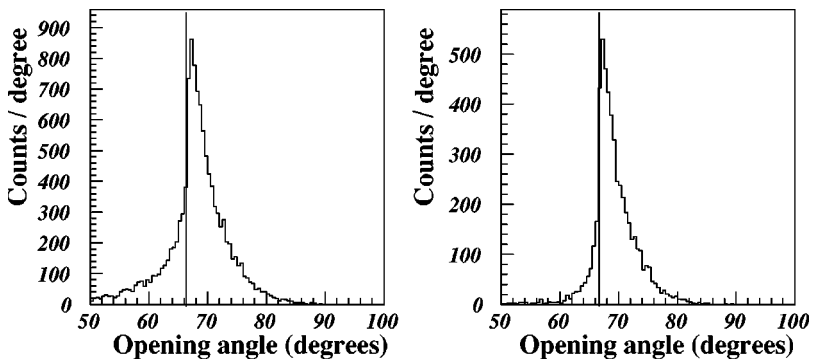

FIG. 12. The left side plot shows the opening angle between two photons without any invariant π^0 mass cut. The right side plot shows the same quantity with an invariant mass cut of FWHM =10 MeV. The vertical line on both plots indicates the kinematical limit of smallest possible opening angle of 66.72°.

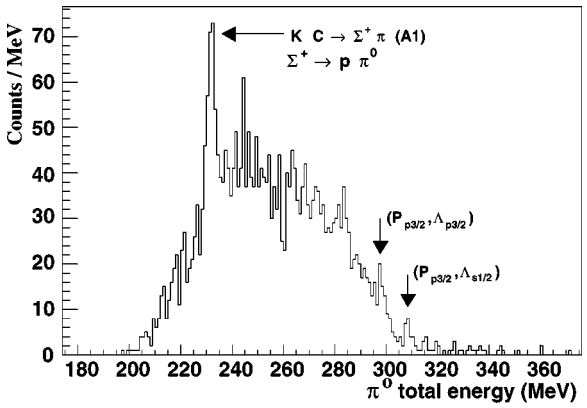

FIG. 13. The entire π^0 energy spectrum, showing the various regions as discussed in the text. The Σ^+ peak is clearly evident in the data.

1. Efficiencies

The efficiency of the ATC was 88% [22], and is defined as the probability with which a kaon can be successfully tracked to its stopped vertex. The NMS efficiency was taken as the percentage with which *both* of the NMS arms provide a tracked conversion point for the photon entering the BGOs. This efficiency was predominantly determined by the NMS wire chambers, and was calculated by comparing the events obtained in the π^0 energy spectrum with and without the requirement that the conversion point of the photon is determined by the NMS wire chambers. An efficiency of $(10\pm2)\%$ was estimated which is in good agreement with Monte Carlo studies of the BGO conversion probabilities and wire chamber hit efficiencies.

The combined data acquisition and analysis efficiency including factors such as computer dead times, and data reduction cuts was estimated to be $(50\pm9)\%$.

2. Acceptance

The *effective acceptance* of the NMS is the geometrical acceptance multiplied by the energy sharing cutoff parameter χ:

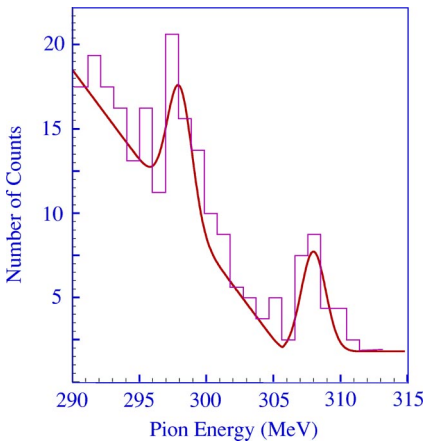

FIG. 14. (Color online) The π^0 energy spectrum near $^{12}_{\Lambda}$B ground state region. The solid line is a fit to the data in the signal region and shows the position and strength of the peaks.

$$\Omega_{effective} = \left| \frac{\Omega}{4\pi} \right|_{\chi cut}. \tag{2}$$

A simple Monte Carlo simulation for various opening angles and pion energies was performed to calculate the $\Omega_{effective}$. The two relevant energies are 245 MeV (for K^+ data) and 307 MeV (for K^- data). At a χ cut of 0.2, $\Omega_{effective}$ (245 MeV)=0.009 14, and $\Omega_{effective}$ (307 MeV) =0.001 15.

E. Branching ratio calculation

The ground state formation probability (or branching ratio) for a bound hypernuclear state $\mathcal{BR}$ is defined as

$$\mathcal{BR} = \frac{\mathcal{N}(P^{-1}_{3/2}, \Lambda_{1/2})}{\mathcal{R}\mathcal{N}_K}. \tag{3}$$

Here $\mathcal{N}(P^{-1}_{3/2}, \Lambda_{1/2})$ is the number of counts in the hypernuclear ground state, $\mathcal{N}_K$ is the number of stopped kaons in the target, and $\mathcal{R}$ describes all other parameters which influence the count rate. The factor $\mathcal{R}$ depends on the effective acceptance, the DAQ efficiency, the ATC efficiency, the NMS overall detection efficiency, and software analysis efficiency. The methods used to obtain the number of stopped kaons as well as the factors influencing $\mathcal{R}$ have been previously described [26]. For the K^- data, $\mathcal{R}$ is calculated to be $(1.33\pm0.20)\times10^{-5}$. The number of stopped kaons is 0.977×10^9. The number of counts $\mathcal{N}(P^{-1}_{3/2}, \Lambda_{1/2})$ was obtained by fitting the ground state peak as discussed in the last section. The total number of counts for the hypernuclear ground state production was estimated at 13.7 ± 4.0. This yields a formation probability of $(0.28\pm0.08)\times10^{-3}$ for the ground state peak. The number of counts for the *p*-shell peak, 17.5 ± 4.5, yields a formation probability of $(0.35\pm0.09)\times10^{-3}$.

The analysis techniques used to analyze the K^- data were also used to analyze the K^+ data. A count rate within 98% of the expected value for the K^+ data was obtained.

F. Discussion of the π^0 spectrum

The full π^0 energy spectrum from the K^- absorption on ^{12}C is shown in Fig. 13. The overall structure of the spectrum is dictated by the NMS solid angle acceptance, pion production kinematics, and subsequent cuts on various quantities.

1. Spectrum shape

The spectrum can be divided into (1) a low-energy region, (2) a region of Σ production, (3) a quasifree Λ production region, (3) a $^{12}_{\Lambda}$B bound state region, and (4) a kinematically unallowed region having pion energies above those for K^- capture at rest to the hypernuclear ground state. The lowest observed total pion energy is determined by the solid angle acceptance of the NMS at an energy sharing parameter value of 0.2. At an opening angle of 55° between the two NMS arms, the effective solid angle approaches zero near 200 MeV as shown in Fig. 15.

The effective acceptance also plays a role in the high-energy end of the spectrum. The effective solid angle, after

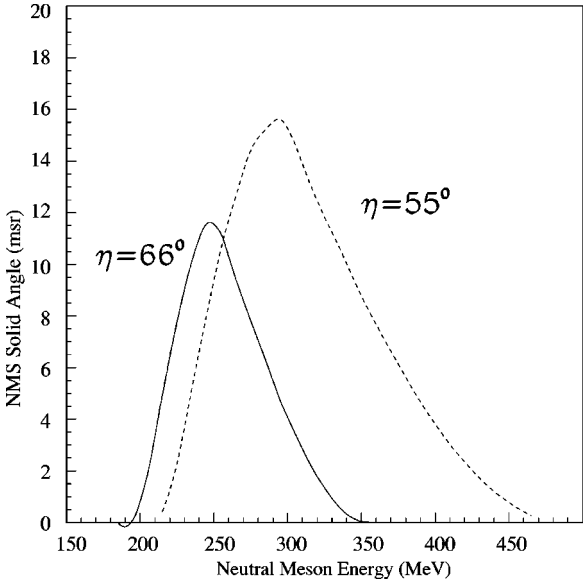

FIG. 15. The NMS solid angle as calculated by Monte Carlo.

peaking near 307 MeV, decreases and approaches zero again at 460 MeV. The region between these extremes is populated by Σ production and the $^{12}_{\Lambda}$B bound state region.

2. Σ^+ peak

A predominant channel of hyperon production in the stopped kaon-nucleus interaction is the Σ channel. The two possible ways of producing π^0's in association with Σ production are

$$K^- + {}^{12}C \rightarrow \Sigma^+ + \pi^- + (A-1),$$

$$\Sigma^+ \rightarrow \pi^0 + p,$$

and

$$K^- + {}^{12}C \rightarrow \Sigma^0 + \pi^0 + (A-1).$$

The π^0's emitted in association with Σ^0's production follow three-body kinematics and have no unique pion emission energies. In contrast, the π^0's produced from Σ^+ decay can be monoenergetic when the Σ^+ decays essentially at rest, and a fraction of the charged Σ's, produced with some recoil momentum, can be brought to rest in the target before they decay. Thus the expected π^0 peak at $\sim$232 MeV associated with a two-body Σ^+ decay at rest is observed in the data. This peak position aids in verifying the energy calibration of the spectrum. The broad structure of the peak is due to Σ^+ decay in flight.

3. Quasifree Λ production

Background π^0's can occur through quasifree Λ production or from Λ decay. However unless significantly boosted, pions from Λ decay have energies either below or near the low-energy cutoff of the NMS acceptance. However π^0's from quasifree Λ production dominate most of the spectrum, whose shape is governed by the NMS acceptance, the Fermi momentum of the interacting protons in the nucleus, and final state interactions between the recoiling particles. Thus this region is composed of a broad momentum distribution of neutral pions.

4. High-energy tails

It is also possible to produce pions with energies above those from the hypernuclear ground state. For example, in-flight K^--nucleus reactions and kaon decays can produce pions in this energy region, although the Lorentz boost requires that energetic pions are forward directed, and therefore their detection is suppressed by the NMS acceptance. However it is also possible that the K^- may be captured on correlated nucleons within the target nucleus, and it has been argued that $\sim$19% of all kaon captures occur with multinucleons participating in the process [29,30]. As an example,

$$K^- + (pp) \rightarrow \Sigma^+ + n,$$

$$\Sigma^+ \rightarrow p + \pi^0.$$

Assuming a simple kinematical model in which the kaon and the two protons are at rest, a Σ^+ of 518 MeV/c momentum is produced, and the decay $\Sigma^+ \rightarrow p + \pi^0$ could produce π^0's across a broad spectrum of energies. This type of background obviously is sensitive to many details of the nuclear capture process as well as the detector and target geometry, and has not been studied in detail here.

5. $^{12}_{\Lambda}B$ states

The interest of this experiment is to investigate the case when the Λ hyperon remains bound to the ^{11}B nuclear core forming a $^{12}_{\Lambda}$B hypernucleus. This is an isospin *mirror* hypernucleus to $^{12}_{\Lambda}$C, which has been previously studied using strangeness exchange and associated production reactions. In mirror nuclei, the exchange of protons and neutrons creates a Couloumb energy shift [31] ΔE_c, however aside from an energy shift of $\sim$1.5 MeV, the level structures should be similar.

Based upon the location of the ground state peak, see Fig. 14, a calculation of the hypernuclear mass and the Λ ground state binding energy can be determined. Using the measured energy of the pion from the ground state peak, E_{π^0} $=308.7\pm1.0$ MeV, the binding energy of the Λ in the $^{12}_{\Lambda}$B nucleus is $B_{\Lambda}=11.2\pm1.0$ MeV, in agreement with the currently accepted value of 11.37 ± 0.06 MeV [32].

6. Backgrounds

The background in hypernuclear production using the $(K^-_{stopped}, \pi^0)$ reaction is larger than in *in-flight* reactions. The $K^-_{stopped}$ reaction is not as selective and the actual momentum of the kaon is only assumed, but not measured, to be zero. In addition, pion momenta from both production and decay products occur in the same spectrum region, and multinucleon captures also produce unavoidable backgrounds.

V. CONCLUSIONS

This study reports on the usefulness of the $^{12}C(K^-_{stopped}, \pi^0)^{12}_{\Lambda}B$ reaction to produce hypernuclei charge

TABLE II. Hypernuclear formation probabilities after stopped K^- capture.

Reference	${}_{\Lambda}S_{1/2}$	${}_{\Lambda}(P_{3/2}+P_{1/2})$
${}^{12}_{\Lambda}$C theory [17]	0.33×10^{-3}	0.96×10^{-3}
${}^{12}_{\Lambda}$C theory [19]	0.12×10^{-3}	0.59×10^{-3}
${}^{12}_{\Lambda}$C theory [21]	0.231×10^{-3}	
${}^{12}_{\Lambda}$C expt. [29]	$(0.98\pm0.12)\times10^{-3}$	$(2.3\pm0.3)\times10^{-3}$
${}^{12}_{\Lambda}$B theory [21]	0.119×10^{-3}	
${}^{12}_{\Lambda}$B expt. (this work)[a]	$(0.28\pm0.08)\times10^{-3}$	$(0.35\pm0.09)\times10^{-3}$

[a]Multiply by 2 to compare this result to ${}^{12}_{\Lambda}$C production.

symmetric to those previously studied by the in-flight (K^-,π^-) and (π^+,K^+) reactions. The ${}^{12}_{\Lambda}$B ground state peak was observed, and an enhancement above a sharply rising background was evident in the region of the expected *p*-shell structure. From the measured pion momenta of the reaction we determine that the Λ binding energy is 11.2 ± 1.0 MeV and the position of the structures is consistent with that expected from its isospin mirror, ${}^{12}_{\Lambda}$C after correction for the Couloumb energy difference.

We find a hypernuclear ground state (g.s.) formation probability of $(0.28\pm0.08)\times10^{-3}$ and that for the *p*-shell of $(0.35\pm0.09)\times10^{-3}$. This is compared in Table II to theoretical and experimental values for the $(K^-_{\text{stopped}},\pi^-)$ reaction which should occur twice as often based on isospin conservation. The quoted errors are statistical, but because of the difficulty in extracting the yield from the background an additional systematic error, somewhat larger for the *p* shell, should also be included. We estimate that the *p*-shell error is about 15%. The formation probability to the ground state is lower than the previous experimental value for ${}^{12}_{\Lambda}$C formation after correction for isospin [29], but remains higher than the theoretical calculations for the ground state [17,19,21].

The energy resolution of the g.s. peak is $\sim$2.2 MeV (FWHM), which is larger than expected, given the measured calorimetry and shower positional resolution. This is attributed to the problems associated in maintaining calibrations over the long period of data acquisition as opposed to the collection of the K^+ data set. The data are not sufficiently accurate to comment on charge asymmetric effects which are expected to be at a level of $\sim$4%.

Finally, given the observed level of background compared to the signal, it appears that the usefulness of this reaction for hypernuclear spectroscopy is limited.

[1] A. Gal and C. B. Dover, Nucl. Phys. **A585**, 1c (1995); J. Schaffner-Bielich, *ibid.* **A639**, 443c (1998).

[2] Proceedings of the Seventh International Conference of Hypernuclear and Strange Particle Physics [Nucl. Phys. **A691**, 1 (2000)].

[3] B. F. Gibson and E. V. Hungerford, Phys. Rep. **257**, 351 (1995).

[4] T. Motoba, in *Mesons and Light Nuclei*, edited by Jiri Adam, Petr Bydzovsky, and Jiri Mares, AIP Conf. Proc. No. 603 (AIP, Melville, NY, 2001), p. 125; E. Hiyama *et al.*, Phys. Rev. C **59**, 2351 (1999).

[5] J. A. Nolen and J. P. Schiffer, Annu. Rev. Nucl. Part. Sci. **19**, 471 (1969).

[6] C. E. Wiegand and D. A. Mack, Phys. Rev. Lett. **18**, 685 (1967).

[7] J. Hüfner, S. Y. Lee, and H. A. Weidenmüller, Nucl. Phys. **A234**, 429 (1974).

[8] M. Jurić *et al.*, Nucl. Phys. **B47**, 36 (1972).

[9] R. H. Dalitz, D. H. Davis, and D. N. Tovee, Nucl. Phys. **A450**, 311c (1986).

[10] B. Povh, Annu. Rev. Nucl. Part. Sci. **28**, 1 (1978).

[11] R. E. Chrien and C. B. Dover, Annu. Rev. Nucl. Part. Sci. **39**, 113 (1989).

[12] C. Milner *et al.*, Phys. Rev. Lett. **54**, 1237 (1985); P. Pile *et al.*, *ibid.* **66**, 2585 (1991).

[13] O. Hashimoto *et al.*, Phys. Rev. Lett. **88**, 042503 (2002).

[14] A. M. Faessler *et al.*, Phys. Lett. **46B**, 468 (1973).

[15] H. Hotichi *et al.*, Phys. Rev. C **64**, 044302 (2001).

[16] H. Tamura, Ph.D. dissertation, University of Tokyo, 1987.

[17] A. Gal and L. Klieb, Phys. Rev. C **34**, 956 (1986).

[18] H. Bando and T. Motoba, Prog. Theor. Phys. **76**, 1321 (1986).

[19] A. Matsuyama and K. Yazaki, Nucl. Phys. **A477**, 673 (1988).

[20] NMS Collaboration, Proposal for a High Resolution Spectrometer for Neutral Mesons, Los Alamos National Laboratory, 1989 (unpublished).

[21] A. Cieplý, E. Friedman, A. Gal, and J. Mareš, Nucl. Phys. **A696**, 173 (2001).

[22] M. Ahmed *et al.*, Nucl. Instrum. Methods Phys. Res. A **469**, 95 (2001).

[23] G. Hogan, PCDaQ Software, Los Alamos National Laboratory.

[24] LeCroy 1997 Research Instrumentation Products Catalog.

[25] L. P. Nguyen, Doctoral dissertation, University of Maryland, 1995, Sec. 3.9.

[26] M. Ahmed, Doctoral dissertation, University of Houston, 1999.

[27] H. Juengst *et al.*, Nucl. Instrum. Methods (submitted).

[28] K. L. Brown and C. Iselin, DECAY TURTLE, a computer program for simulating charged particle beam transport systems, including decay calculations, CERN 74-2, 1974.
[29] H. Tamura (private communication).
[30] C. Vander Vale-Wilquet, J. Scaton, and J. H. Wickens, Nuovo Cimento Soc. Ital. Fis., A **39A**, 538 (1977).
[31] K. S. Krane, *Introductory Nuclear Physics* (Wiley, New York, 1988).
[32] P. Dluzewski *et al.*, Nucl. Phys. **A484**, 520 (1988).